Numerical simulation of magnetic compression on a field-reversed configuration plasma

T. Kanki, Y. Suzuki, S. Okada, and S. Goto

View Online   Export Citation

ARTICLES YOU MAY BE INTERESTED IN

Review of field-reversed configurations
Physics of Plasmas **18**, 070501 (2011); https://doi.org/10.1063/1.3613680

Magnetohydrodynamic simulation of dynamical behavior of a field-reversed configuration during magnetic mirror reflection
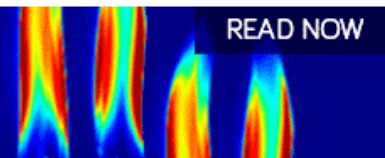Physics of Plasmas **10**, 3635 (2003); https://doi.org/10.1063/1.1600735

Adiabatic compression of elongated field-reversed configurations
The Physics of Fluids **26**, 1564 (1983); https://doi.org/10.1063/1.864334

Numerical simulation of magnetic compression on a field-reversed configuration plasma

T. Kanki,[a)] Y. Suzuki, S. Okada, and S. Goto
Plasma Physics Laboratory, Graduate School of Engineering, Osaka University, 2-1 Yamada-oka, Suita, Osaka 565-0871, Japan

A two-dimensional magnetohydrodynamic (MHD) simulation of an axial magnetic compression on a field-reversed configuration (FRC) plasma is carried out for the parameter range of a corresponding experiment conducted on the FRC Injection Experiment (FIX) [S. Okada *et al.*, *17th IAEA Fusion Energy Conference 1998* (International Atomic Energy Agency, Vienna) (in press)]. The simulation results show that during the initial stage of the magnetic compression the front part of the FRC plasma is mainly compressed radially, and that after this stage, the compression is primarily axial. Of particular interest is expected that the closed magnetic flux surfaces of the FRC can be retained without any degradation during the magnetic compression process. Further, it is observed in the simulation that the axial magnetic compression enables a transition of the MHD equilibrium from a long and thin to a short and fat FRC. The effects of this magnetic compression on FRC plasmas are discussed. © *1999 American Institute of Physics.* [S1070-664X(99)01812-1]

I. INTRODUCTION

A field-reversed configuration (FRC) (Ref. 1) is an elongated compact toroid with intrinsically high plasma beta. It also has the attractive feature of having no material objects linking the torus, which allows the FRC, formed by the theta-pinch method, to be translated along the cylindrical axis and easily compressed in a vacuum chamber by using auxiliary coils. Magnetic compression is particularly well suited for FRC plasmas,[2] and a new magnetic compression method has been proposed.[3] This method is an axial magnetic compression, which can possibly be used to control the equilibrium and improve the confinement of FRC plasmas. Axial magnetic compression of FRC plasmas is accomplished by shortening the distance between a pair of magnetic mirror fields in the confinement region. This compression results in the increase of the separatrix radius r_s and the decrease of the separatrix length l_s. In general, the large plasma radius will improve the magnetic decay and particle loss times.[4,5] This improved confinement can be explained by the empirical scaling law, $\tau_N \propto R^2/\rho_i$.[6] Here τ_N, R, and ρ_i represent the particle confinement time, the FRC major radius, and the ion gyro radius in the external magnetic field, respectively.

On the FRC Injection Experiment (FIX) machine[7,8] at Osaka University, the axial compression magnetic field is produced by 3-turn coils installed coaxially in the confinement vessel, i.e., the magnetic compression field is applied to the FRC which eventually settles down in the confinement region. In this experiment, it has been observed that the separatrix radius increases by about 10%, and that the plasma is axially compressed by about 30%. As a result, the FRC's lifetime of about 500 μs can be extended by approximately 50 μs.[9] However, the details of how the compression process works remain unclear.

Specifically, it is difficult to experimentally measure the separatrix radius in the vicinity of the magnetic compression coils when the compressing field is applied to the FRC. This is because the axial array of magnetic field probes, used for the excluded flux measurement, lies outside of the axial compression coil set, and so measures both the compressing and the confining fields. Thus, the separatrix shape of the FRC in the vicinity of the compression coils is poorly known.

There are also important questions related to the confinement and magnetohydrodynamic (MHD) stability of the compressed FRC: (1) Can the closed flux surfaces be retained during the magnetic compression process? (2) Is it possible to control the MHD equilibrium configuration? (3) How are the separatrix shape and current profile changed before and after compression? In future we wish to explore a new range of equilibria, not previously considered, that is accessible by magnetic compression, and which may have properties that improve the confinement and stability of FRC plasmas.

In order to answer the questions stated above, we investigate the fundamental physics of this magnetic compression process by means of an axisymmetric numerical simulation. In this paper, we focus our attention on the effects of the applied compressing magnetic field on FRC plasmas. Furthermore, we explore whether the equilibrium configurations and radial profiles of the FRC can be controlled by an external compressing magnetic field. For this purpose, we have developed a two-dimensional MHD simulation code. In Sec. II, we describe our simulation model. In Sec. III, simulation results are presented, and in Sec. IV a summary and discussion are given.
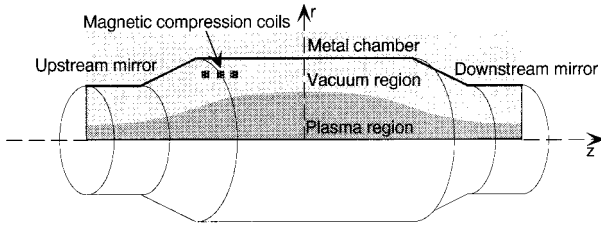
[a)]Electronic mail: kanki@ppl.eng.osaka-u.ac.jp

FIG. 1. Schematic view of the computation domain in cylindrical coordinates (z,r,ϕ), corresponding to the confinement region in the FIX machine. The shaded poloidal plane represents the two-dimensional simulation region.

II. SIMULATION MODEL

A. Model of confinement region

As shown in Fig. 1, the confinement region of the FIX machine consists of a central region with mirror field regions at either end.[8,9] The central confinement region is a 0.8 m inner diameter and 3 m long metal chamber. The confining magnetic field in this region is generated by quasi-dc coils. The strength of this magnetic field in vacuum B_0 ranges from 0.01 to 0.08 T. In our simulation, we fix B_0 at 0.04 T, which is a typical value. Both ends of the confinement region taper away to mirror field regions with an inner diameter of 0.5 m. The strength of the upstream and downstream magnetic mirror fields B_m are 0.13 and 0.17 T, respectively. In the simulation, however, we assume that the confining magnetic flux in the central region is the same as in the mirror field region at either end. Hence, in accordance with $B_0 = 0.04$ T, we set $B_m = 0.1$ T as the strength of the mirror field.

The magnetic compression coils are installed coaxially in the confinement region. The three-turn compression coils are 0.66 m in diameter and are equispaced at 0.2 m intervals, as shown in Fig. 1. The strength of the maximum compressing magnetic field B_c varies from 0.05 to 0.1 T, and the typical rise time is about 30 μs. The operation model in the simulation for the compressing magnetic field is shown in Fig. 2.
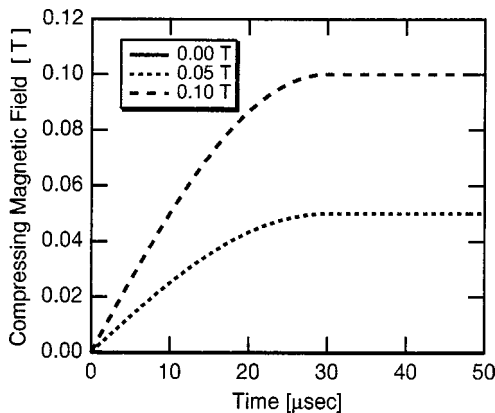

FIG. 2. Operation model for the compressing magnetic field, produced by the magnetic compression coils. This magnetic field rises sinusoidally between 0 and 30 μs, and is thereafter kept constant.

B. Governing equation and boundary conditions

We use a cylindrical coordinate system (z,r,ϕ) in which the z-axis lies along the symmetry axis of the confinement chamber. We assume axisymmetry, and carry out numerical simulations in a two dimensional (z,r) plane. As shown in Fig. 1, we divide the domain in which the simulation is performed into two regions. One is a vacuum subregion where only the magnetic field is calculated, and the other is a plasma subregion where the full set of MHD equations are solved. We use a perfect conducting boundary at the chamber wall. Further, free boundary conditions are imposed on the open ends of the confinement region, in order to reduce the reflection of MHD flow. Since in general, a FRC has sharp plasma pressure gradients in the vicinity of the separatrix, we employ a Lagrangian mesh, so as to allow a concentration of the mesh in that region.[10–13] Furthermore, a two temperature MHD model,[14] which calculates electron and ion temperatures separately, is used, because the electron–ion energy transfer time in the confinement region is much longer than the time scale of the compression. The Lagrangian MHD equations are as follows:

$$\frac{d\rho}{dt} = -\rho \mathbf{\nabla} \cdot \mathbf{v}, \tag{1}$$

$$\frac{d\mathbf{v}}{dt} = \frac{1}{\rho}[-\nabla p + \mathbf{j} \times \mathbf{B}], \tag{2}$$

$$\frac{d\mathbf{B}}{dt} = (\mathbf{B} \cdot \mathbf{\nabla})\mathbf{v} - \mathbf{B}(\mathbf{\nabla} \cdot \mathbf{v}) - \mathbf{\nabla} \times (\eta \mathbf{j}), \tag{3}$$

$$\frac{d\epsilon_i}{dt} = \frac{1}{\rho_i}[-p_i(\mathbf{\nabla} \cdot \mathbf{v}) - \mathbf{\nabla} \cdot \mathbf{q}_i + Q_i], \tag{4}$$

$$\frac{d\epsilon_e}{dt} = \frac{1}{\rho_e}[-p_e(\mathbf{\nabla} \cdot \mathbf{v}) - \mathbf{\nabla} \cdot \mathbf{q}_e + Q_e], \tag{5}$$

where $\rho(=\rho_e + \rho_i)$ is total mass density, $\mathbf{v}$ is fluid velocity, $\mathbf{B}$ is magnetic field, $\mathbf{j}(=\mathbf{\nabla} \times \mathbf{B}/\mu_0)$ is electrical current density, $\epsilon(=\epsilon_e + \epsilon_i)$ is total specific internal energy, $p(=p_e + p_i)$ is total pressure, $\mathbf{q}(=\mathbf{q}_e + \mathbf{q}_i)$ is total heat flow, and η is the electrical resistivity due to classical electron collisions. In addition, ρ_α, p_α, ϵ_α, and $\mathbf{q}_\alpha$ refer to the appropriate electron or ion quantities, and Q_i and Q_e represent the Braginskii electron-ion energy equilibration and Joule heating terms.[15] The effects of unequal parallel and perpendicular thermal conduction, which follow Braginskii, are included for both the electrons and the ions.[15]

C. Numerical method

In this subsection, we explain the numerical method used in the MHD simulation.[16] First, we consider the calculation of the vacuum subregion. The vacuum flux ψ_v is calculated by solving the following equation for the static magnetic field,

$$\mathcal{L}\psi_v = -\mu_0 r j_\phi, \tag{6}$$

where $\mathcal{L}$ is the differential operator defined by
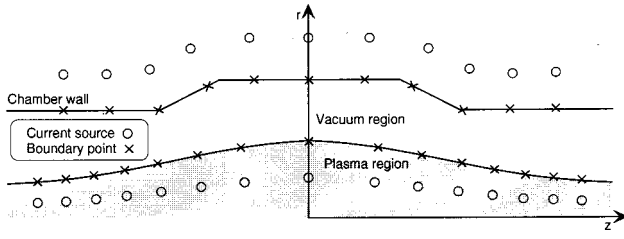
FIG. 3. Arrangement of the current sources and the boundary points.

$$\mathcal{L} \equiv r \frac{\partial}{\partial r}\left(\frac{1}{r}\frac{\partial}{\partial r}\right) + \frac{\partial^2}{\partial z^2}, \tag{7}$$

and j_ϕ is the toroidal component of the current density. The vacuum solution ψ_v of Eq. (6) is given by

$$\psi_v(z,r) = \sum_{i=1}^{N} \lambda_i G(z,r;z_i,r_i), \tag{8}$$

where λ_i ($i=1,...,N$) is the value of a current ring at the point (z_i,r_i), and the fundamental solution G is written as

$$G(z,r;z_i,r_i) = \frac{\mu_0}{2\pi}\frac{\sqrt{r_i r}}{k}\left[(2-k^2)K(k) - 2E(k)\right], \tag{9}$$

where $K(k)$ and $E(k)$ denote the complete elliptic integrals of the first and second kind, respectively, and k is defined by

$$k^2 \equiv \frac{4r_i r}{(r+r_i)^2 + (z-r_i)^2}. \tag{10}$$

The vacuum flux ψ_v is determined in such a way that Eq. (8) can satisfy the appropriate boundary conditions at the chamber wall and the vacuum-plasma interface. Dividing the boundaries into M points, we arrange the N virtual current sources in the plasma subregion and outside the chamber as shown in Fig. 3. Consequently, the vacuum flux ψ_v is estimated from a set of parameters λ_i ($i=1,...,N$), determined by solving the nonlinear least squares problem,

$$\chi = \sum_{j=1}^{M}\left[\psi_v(z_j,r_j) - b_j\right]^2, \tag{11}$$

through Simplex and Marquardt methods.[17] Here b_j ($j=1,...,M$) are the values of ψ_v on the boundaries.

Next, we consider the calculation of the plasma subregion. First of all, the effects of dissipation terms such as the resistive diffusion of the magnetic field, the Joule heating and the thermal conduction are described. The resistive diffusion of the magnetic field is solved explicitly since it proceeds on a very slow time scale compared to fluid motion. Therefore, the explicit difference equations for resistive diffusion terms are solved before performing the no-dissipation (adiabatic) calculation. The numerical procedure is comprised of three steps. In the first step, the current density at each vertex in the computation mesh is obtained by applying Ampère's Law. In the second step, the magnetic field diffusion caused by current flow is calculated by using the current density obtained in the first step. In the third step, the Joule heating is calculated and added to the internal energy. Following the calculation of the field diffusion, the equations of

thermal conduction are solved in implicit form because these equations deal with the nonlinear electron thermal diffusion process.[18] The implicit difference equations for thermal conduction are calculated by using the successive over-relaxation (SOR) method. As boundary conditions of these equations, it is assumed that the heat flux at the vacuum–plasma interface is zero, and that the heat transport at both open ends is done freely.

Here, we consider the numerical method on the basis of a calculation reported by Brackbill and Pracht[11] for solving Eqs. (1)–(5), except for the dissipation terms stated above. In order to satisfy these equations consistently, we employ an iterative procedure. The variation of each physical variable during a Lagrangian time step δt can be calculated implicitly. Mesh vertices of cell a must be moved with the fluid to their new positions,

$$\mathbf{r}^{(n+1)} = \mathbf{r}^{(n)} + \mathbf{v}\delta t, \tag{12}$$

where the superscript $(n+1)$ and (n) represent time-advanced and previous time values, respectively. Then, the volume of cell a at the previous time $V_a^{(n)}$ is changed to the new volume $V_a^{(n+1)}$ according to Eq. (12). By using Eqs. (1), (4), and (5) without dissipation terms, the new density and pressure in cell a can be approximated in terms of initial values as

$$\rho_a^{(n+1)} = \rho_a^{(n)}\frac{V_a^{(n)}}{V_a^{(n+1)}}, \tag{13}$$

$$p_a^{(n+1)} = p_a^{(n)}\left[\frac{V_a^{(n)}}{V_a^{(n+1)}}\right]^{\gamma}, \tag{14}$$

where γ is the ratio of specific heats ($\gamma=5/3$). In this process, the mass in cell a can be conserved, and the adiabatic relation can be satisfied there. In other words, this process ensures that the iterative solutions of density and pressure satisfy Eqs. (1), (4), and (5) automatically. As a result of the above process, the problem can be solved, by an iterative procedure, to estimate $\mathbf{B}^{(n)}$ and $\mathbf{v}^{(n)}$. This consists of two steps. In the first step, the iterative solution for magnetic field $\mathbf{B}^{(n)}$ is determined by solving the implicit equations for Eq. (3) through the Newton–Raphson method.[17] Subsequently, using $\mathbf{B}^{(n)}$ obtained in the first step, we update the iterative solution of velocity $\mathbf{v}^{(n)}$ by estimating the right-hand side of Eq. (2). The final numerical solution for Eqs. (2) and (3) is obtained after these two steps have been iterated sufficiently for $\mathbf{B}^{(n)}$ and $\mathbf{v}^{(n)}$ to satisfy suitable convergence criteria. Further, in our MHD code, mesh rezoning[13] is employed in the case that the movement of fluid gives rise to distortion of the mesh.

Finally, an initial condition for the simulation is described as follows. We use an axisymmetric MHD equilibrium of a FRC (Ref. 19) as an initial value for the simulation. The MHD equilibrium of a FRC is described by the Grad–Shafranov equation for the poloidal flux function ψ,

$$\mathcal{L}\psi = -r^2\frac{dp}{d\psi}, \tag{15}$$

TABLE I. Parameter for initial plasma conditions.

Separatrix radius r_s	0.17 m
Separatrix length l_s	3.15 m
Average mass density ρ	2.2×10^{-7} kg/m³
Axial velocity v_z	0.0 m/μs
Radial velocity v_r	0.0 m/μs
Ion temperature T_i	50.0 eV
Electron temperature T_e	50.0 eV
Confining magnetic field B_0	0.04 T

where p denotes the plasma pressure. In order to solve Eq. (15) numerically under the boundary conditions in the region indicated in Fig. 1, a profile of $dp/d\psi$ must be assumed. As the profile, we take

$$\frac{dp}{d\psi} = \begin{cases} -c(1+\xi\psi) & \text{for } \psi < 0, \\ -cd & \text{for } 0 \leq \psi < \psi_0, \\ 0 & \text{for } \psi_0 \leq \psi. \end{cases} \quad (16)$$

Here c, ξ, and d are constants, and ψ_0 is the value of ψ on the vacuum–plasma interface. Note that in Eq. (16) we have $\psi < 0$ inside the separatrix and $\psi \geq 0$ outside the separatrix. FRC equilibria are given by solving the finite difference equation for Eq. (16) using the SOR method; details are found in Ref. 20. As the initial value for the simulation, we use a numerically computed equilibrium with separatrix radius (normalized by the wall radius at $z=0$) $x_s \simeq 0.4$, such as is typically observed in the FIX experiment. By applying the thermodynamic equation of an ideal fluid, the plasma density profile can be estimated, assuming that the temperature is spatially uniform in the plasma region. The parameters of the initial condition for the simulation are presented in Table I.

III. SIMULATION RESULTS

On the basis of the simulation results, the effects of a compressing magnetic field on a FRC plasma are investigated. Poloidal flux contours of the FRC with an applied compressing magnetic field of 0.05 T are shown in Fig. 4, where both the plasma and vacuum regions are plotted. The top panel in Fig. 4 shows the initial poloidal flux contours before the compression stage, which are an equilibrium of the FRC. In the initial stage of the compression process ($t < 10\,\mu$s), one can see that the front part of the FRC is mainly compressed radially by the compressing magnetic field. During this stage, a part of the FRC that seems to swell is the shoulder. After this stage, the FRC is primarily compressed axially. In particular, the separatrix shape near the axis is substantially deformed due to a strong axial plasma flow as shown at $t = 30\,\mu$s. The axial magnetic compression of the FRC has been completed at about $t = 40\,\mu$s. Therefore, the magnetic compression process leads the initial long and thin FRC ($r_s = 0.17$ m, $l_s = 3.15$ m) to the final more short and fat FRC ($r_s = 0.19$ m, $l_s = 2.60$ m). More interestingly, the behavior is expected that the closed magnetic flux surfaces of the FRC can be retained without any degradation during the magnetic compression process. Furthermore, the X-point of the upstream side moves toward the downstream due to the axial magnetic compression, whereas that of the
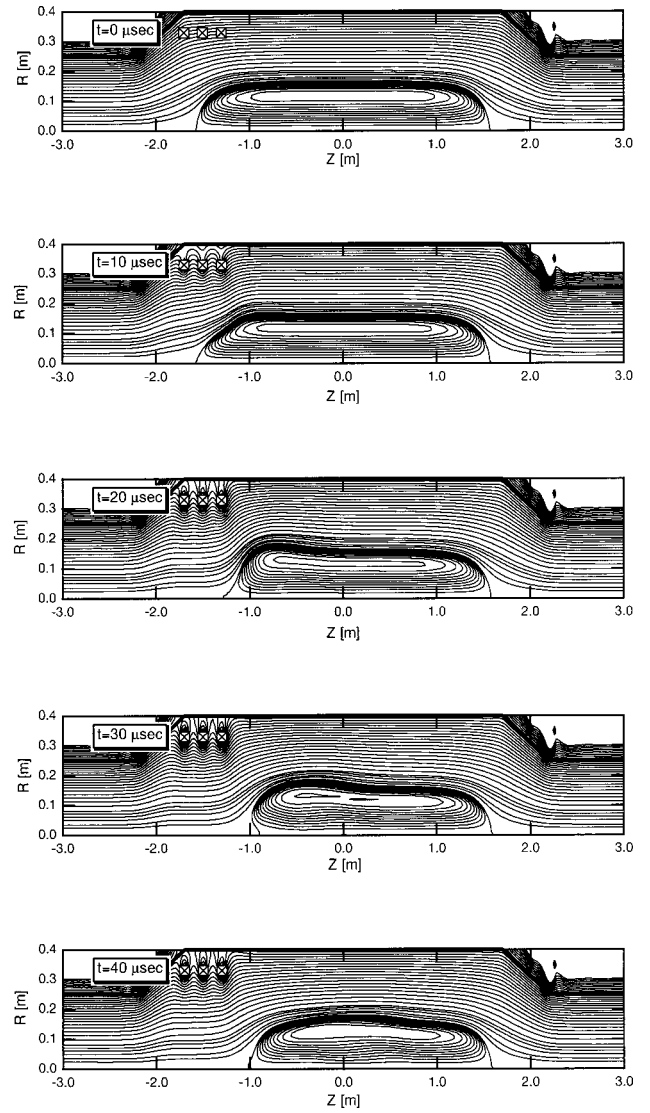

FIG. 4. Time evolution of the poloidal flux contours of the FRC at an applied compressing magnetic field of 0.05 T.

downstream side hardly moves. This result suggests that the motion of the FRC is different from a rigid body model.

Figure 5 shows the temporal plots of the radius and length of the separatrix, and $\langle \beta \rangle$, the beta value spatially averaged inside the separatrix, when the strength of the applied compressing magnetic field is changed. It is seen from Fig. 5 that the onset time of each physical quantity is almost independent of the strength of the applied compressing field, and that after compression, each quantity approaches a given value. The difference in the magnitude of each physical quantity is not very sensitive to the intensity of the applied compressing field. This result reflects the fact that the FRC is axially compressed using a compressing magnetic field ($\simeq 0.05$ T) of similar strength to that of the confining magnetic field ($\simeq 0.04$ T). Furthermore, each physical quantity is not changed in the initial stage of the compression process ($t < 10\,\mu$s). This implies that the quantities are influenced by axial compression, not radial. By quantitatively estimating the radius and length of the separatrix from Figs. 5(a) and 5(b), we observe that there is about a 13% increase in the
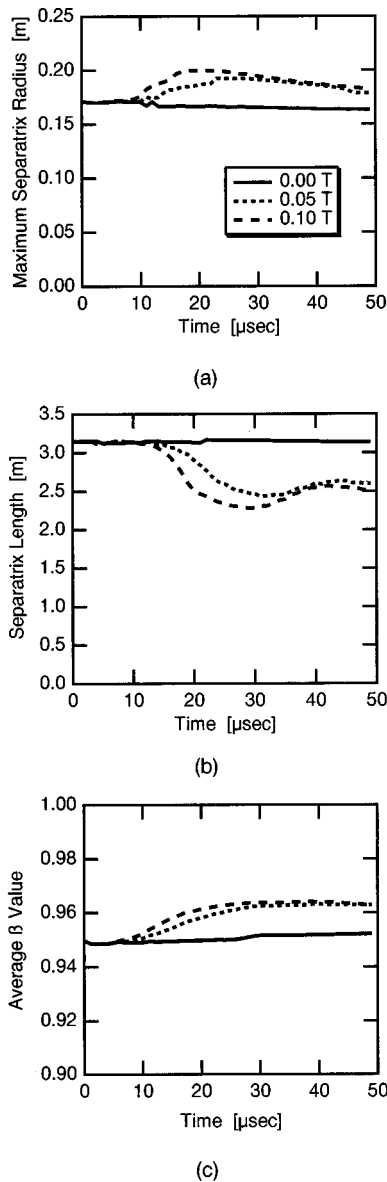
FIG. 5. Time evolution of several important physical quantities when the strength of the applied compressing magnetic field is changed; (a) maximum separatrix radius r_s; (b) separatrix length l_s; (c) beta value spatially averaged inside of the separatrix $\langle\beta\rangle$.

FIG. 6. Time evolution of the spatially averaged force $\langle|\mathbf{j}\times\mathbf{B}-\nabla p|\rangle$ for the same conditions as Fig. 4. Here $\mathbf{j}$, $\mathbf{B}$, and p denote the current density, magnetic field, and plasma pressure, respectively. The dotted line shows the axial component of this quantity.

netic field and the end mirror field appears in the case where the plasma is not sufficiently extended into the end mirror region. In that case, in the absence of a compressing field, the FRC is hardly effected by the end mirror fields. With the addition of a compressing field however, the mirror fields can influence the FRC.

In order to examine the motion of the FRC during the magnetic compression process, we plot the temporal evolution of the spatially averaged force $\langle|\mathbf{j}\times\mathbf{B}-\nabla p|\rangle$ in Fig. 6. Between $t=0$ and 15 μs the FRC is axially accelerated, while exhibiting a dynamic radial bouncing motion. After $t=15$ μs the average force approaches zero, and the MHD equilibrium condition of $\mathbf{j}\times\mathbf{B}=\nabla p$ is approximately satisfied after $t=30$ μs.

Figures 7 and 8 show the radial profiles of the plasma pressure and the toroidal current density on the midplane before (at $t=0$ μs) and after compression (at $t=40$ μs). It is seen from Fig. 7 that the increased pressure profile due to the magnetic compression is broadened in the peaked part. In addition, the pressure gradients near the separatrix after compression are sharper than those before compression. It is seen from Fig. 8 that the toroidal current density profile after compression is more hollow than that before compression. The discontinuity in the current density profile outside the separatrix before compression is due to the initial assumption of $dp/d\psi$. Some of the changes in the current profile are due to a resistive relaxation. As a result of it, the discontinuity becomes continuous there. Note that the more hollow current

separatrix radius and about a 23% decrease in the separatrix length in the case of an applied compressing magnetic field of 0.05 T. The axial compression velocity obtained by the temporal evolution of the separatrix length is about 0.04 m/μs. This velocity is almost the same as the Alfvén velocity. From Fig. 5(c) we consider the effect of the compressing magnetic field on the average beta. It is found that the increase in the average beta is caused by this magnetic field. For example, for an applied magnetic field of 0.05 T, this increase is about 1%. The higher values of $\langle\beta\rangle$ make the plasma more unmagnetized, implying increased kinetic effects and transport. This effect of the compressing magnetic field on the average beta is analogous to that of the end magnetic mirrors. The latter case has been discussed within the limit of MHD equilibrium theory.[21,22] The difference, in their influence on the FRC, between the compressing mag-
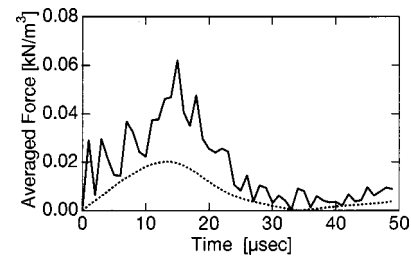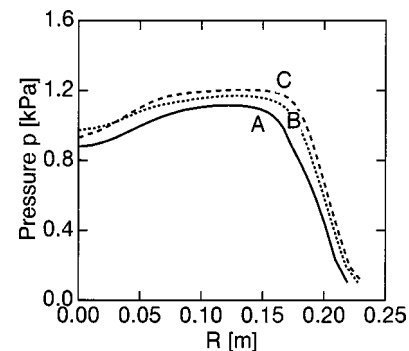
FIG. 7. Radial plasma pressure profiles at the midplane where A represents the equilibrium profile before compression (solid line), B the result of a two-turn coil compression (dotted line), and C the result of a three-turn coil compression (dashed line).
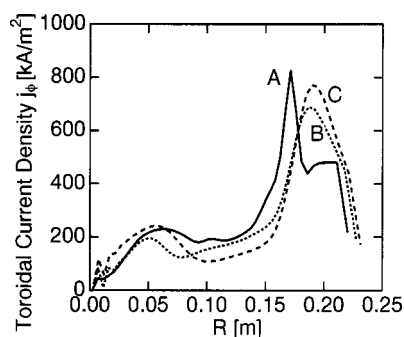
FIG. 8. Radial toroidal current density profiles at the midplane where A represents the equilibrium profile before compression (solid line), B the result of a two-turn coil compression (dotted line), and C the result of a three-turn coil compression (dashed line).

density profile corresponds to the broader (at the magnetic axis) pressure profile.

As stated above, it is confirmed from Fig. 6 that the equilibrium condition can be satisfied before and after compression. Therefore, in order to evaluate the influence of the compressing magnetic field on the equilibrium shape and radial current profile, three equilibrium characteristics are introduced. These are the separatrix elongation, E, the shape index, N (denoting the separatrix shape in the end region) and the current profile index, h (denoting the structure of the current profile).[23] An N value nearly equal to E reflects an elliptical separatrix, while an N value less than E describes a racetrack separatrix. Furthermore, equilibria with $h=1$ are designated as having a flat current profile; $h<1$ as hollow, and $h>1$ as peaked. These macroscopic quantities obtained from Figs. 4 and 8 are $E=9.2$, $N=6.0$, and $h=0.55$ before compression (at $t=0\ \mu\mathrm{s}$), and $E=7.0$, $N=7.1$ and $h=0.35$ after compression (at $t=40\ \mu\mathrm{s}$). Here, N values are estimated from the separatrix shape on the upstream side. The separatrix shape for this case changes from racetrack to elliptical, whereas the current profile becomes more hollow. The increase in N is ascribed to the strength of the compressing magnetic field being weaker than that of the initial mirror field. In the case of an applied compressing magnetic field of 0.05 T, the mirror ratio at the upstream side is changed from 2.56 to 2.25.

IV. SUMMARY AND DISCUSSION

An axisymmetric MHD simulation code has been used to model the dynamics of a magnetic compression process on a FRC plasma. As an initial state we use a MHD equilibrium configuration such as is typically observed in the FIX experiment. Then a compressing magnetic field is applied to this FRC equilibrium. The numerical results obtained in this paper are summarized as follows:

(1) The magnetic compression consists of two stages. During the initial stage the front part of the FRC plasma is mainly compressed radially; after that the compression is primarily axial. The axial magnetic compression process leads the initial long and this FRC to the final more short and fat FRC. The behavior is expected that the closed

magnetic flux surfaces of the FRC can be successfully retained without any degradation during the magnetic compression process.

(2) The X-point of the upstream side moves toward the downstream due to the axial magnetic compression, whereas that of downstream side hardly moves. This result suggests that the motion of the FRC plasma is different from a rigid body model.

(3) The FRC plasma is axially compressed using a compressing magnetic field ($\simeq 0.05$ T) similar in strength to that of the confining magnetic field ($\simeq 0.04$ T).

(4) The increase in the average beta is caused by the compressing magnetic field. The higher beta value makes the plasma more unmagnetized, implying increased kinetic effects and transport. This effect of the compressing magnetic field on the average beta is analogous to the effects of the end magnetic mirrors.

(5) By examining the motion of the FRC plasma during the magnetic compression process, it is found that the MHD equilibrium condition is approximately satisfied before and after magnetic compression. It is then possible to discuss the effects of the magnetic compression on the equilibrium quantities.

(6) The increased pressure profile due to magnetic compression is broadened in the peaked part, while the toroidal current density profile after compression is more hollow than that before compression. For an applied compressing magnetic field of 0.05 T, the separatrix shape changes from racetrack before compression to elliptical after compression.

In the following, on the basis of the above simulation results, we will discuss the control of the equilibrium shape and the radial profile using the compressing magnetic field. The simulation results suggest that the equilibrium shape and radial profile (i.e., pressure and current) can be well-controlled by the externally applied compressing field. These results are analogous to the effects of the magnetic mirrors at the ends of FRCs. However, axial magnetic compression could make available a wider variety of equilibrium shapes and radial profiles than that due to the mirror fields alone. These new equilibria represent an *extended equilibrium space* obtainable through the application of axial magnetic compression. Such new equilibria are of interest for studies of stability and confinement in FRC's.

[1] M. Tuszewski, Nucl. Fusion **28**, 2033 (1988).

[2] D. J. Rej, D. P. Taggart, M. H. Baron, R. E. Chrien, R. J. Gribble, M. Tuszewski, W. J. Waganaar, and B. L. Wright, Phys. Fluids B **4**, 1909 (1992).

[3] S. Okada, M. Ohnishi, Y. Tomita, and H. Momota, in *Proceedings of the 1996 International Conference on Plasma Physics*, Nagoya, 1996 (The Japan Society of Plasma Science and Nuclear Fusion Research, Nagoya, 1997), p. 1182.

[4] M. Tuszewski and R. K. Linford, Phys. Fluids **25**, 765 (1982).

[5] M. Tuszewski, W. T. Armstrong, R. R. Bartsch, R. E. Chrien, J. C. Cochrane, R. W. Kewish, P. L. Klingner, R. K. Linford, K. F. McKenna, D. J. Rej, E. G. Sherwood, and R. E Siemon, Phys. Fluids **25**, 1696 (1982).

[6] K. F. McKenna, W. T. Armstrong, R. R. Bartsch, R. E. Chrien, J. C. Cochrane, R. W. Kewish, P. L. Klingner, R. K. Linford, D. J. Rej, E. G. Sherwood, R. E Siemon, and M. Tuszewski, Phys. Rev. Lett. **50**, 1787 (1983).

[7] H. Himura, S. Okada, S. Sugimoto, and S. Goto, Phys. Plasmas **2**, 191 (1995).

[8] K. Kitano, H. Matsumoto, K. Yamanaka, F. Kodera, S. Yoshimura, S. Sugimoto, S. Okada, and S. Goto, in *Proceedings of the 1998 International Congress on Plasma Physics Combined with the 25th European Physical Society Conference on Controlled Fusion and Plasma Physics*, Praha, 1998 (European Physical Society, Petit-Lancy, 1998), Vol. 22C, p. 886.

[9] S. Okada, K. Kitano, H. Matsumoto, K. Yamanaka, T. Ohtsuka, A. Martin, M. Okubo, S. Yoshimura, S. Sugimoto, S. Ohi, and S. Goto, ''Axial compression of a FRC plasma,'' in *Proceedings of the 17th IAEA Fusion Energy Conference, 1998* (International Atomic Energy Agency, Vienna, in press).

[10] W. D. Schulz, in *Methods in Computational Physics*, edited by B. Alder, S. Fernbach, and M. Rotenberg (Academic, New York, 1964), Vol. 3, p. 1.

[11] J. U. Brackbill and W. E. Pracht, J. Comput. Phys. **13**, 455 (1973).

[12] J. U. Brackbill, in *Methods in Computational Physics*, edited by B. Alder, S. Fernbach, and M. Rotenberg (Academic, New York, 1976), Vol. 16, p. 1.

[13] J. U. Brackbill and J. S. Saltzman, J. Comput. Phys. **46**, 342 (1982).

[14] R. D. Milroy and J. U. Brackbill, Phys. Fluids **25**, 775 (1982).

[15] S. I. Braginskii, in *Review of Plasma Physics* (Consultants Bureau, New York, 1965), Vol. 1, p. 205.

[16] N. Mizuguchi (private communication, 1997).

[17] W. H. Press, S. A. Teukolsky, W. T. Vetterling, and B. P. Flannery, *Numerical Recipes in* FORTRAN, 2nd ed. (Cambridge University Press, New York, 1992).

[18] Ya. B. Zeldovich and Yu. P. Raizer, *Physics of Shock Waves and High-Temperature Hydrodynamic Phenomena 2* (Academic, New York, 1966).

[19] D. W. Hewett and R. L. Spencer, Phys. Fluids **26**, 1299 (1983).

[20] Y. Suzuki, S. Sugimoto, S. Okada, and S. Goto, Technol. Rep. Osaka Univ. **46**, 143 (1996).

[21] K. Suzuki and S. Hamada, J. Phys. Soc. Jpn. **53**, 16 (1984).

[22] R. L. Spencer and M. Tuszewski, Phys. Fluids **28**, 1810 (1985).

[23] L. C. Steinhauer, A. Ishida, and R. Kanno, Phys. Plasmas **1**, 1523 (1994).